

## Isotope and trace element characteristics of a super-fast spreading ridge: East Pacific rise, 13–23°S

J.J. Mahoney <sup>a</sup>, J.M. Sinton <sup>a</sup>, M.D. Kurz <sup>b</sup>, J.D. Macdougall <sup>c</sup>, K.J. Spencer <sup>a</sup>,  
G.W. Lugmair <sup>c</sup>

<sup>a</sup> School of Ocean and Earth Sciences and Technology, University of Hawaii, Honolulu, HI 96822, USA

<sup>b</sup> Woods Hole Oceanographic Institution, Woods Hole, MA 02543, USA

<sup>c</sup> Scripps Institution of Oceanography, University of California, San Diego, CA 92093, USA

(Received May 27, 1993; revision accepted October 25, 1993)

### Abstract

Isotopic patterns of Nd, Sr, and Pb are remarkably coherent along the super-fast spreading portion of the East Pacific Rise from 13°S to 23°S. Between 15.8°S and 20.7°S, all three define a broad, smooth peak, which culminates at ~17–17.5°S and is characterized by elevated  $^{87}\text{Sr}/^{86}\text{Sr}$ ,  $^{206}\text{Pb}/^{204}\text{Pb}$ , and lower  $\epsilon_{\text{Nd}}$  (reaching values of 0.70271, 18.64, and +8.9, respectively). To the north and south this peak is flanked by ~300 km long, isotopically homogeneous sections of ridge with higher  $\epsilon_{\text{Nd}}$  (~+10.9) and lower  $^{87}\text{Sr}/^{86}\text{Sr}$  (~0.7024) and  $^{206}\text{Pb}/^{204}\text{Pb}$  (~18.1). Although otherwise similar, these two sections differ from each other slightly in their  $^{207}\text{Pb}/^{204}\text{Pb}$  and  $^{87}\text{Sr}/^{86}\text{Sr}$  ratios. The isotopic peak corresponds to a region of greater axial cross-sectional area, but axial bathymetry and physical segmentation appear generally unrelated to mantle isotopic composition. However, an abrupt break in isotopic ratios does occur at the large, > 3 Ma, southward-propagating overlapping spreading center at 20.7°S, which marks the end of the south limb or flank of the isotopic peak. The peak itself appears to be a manifestation of large-scale binary mixing between material possessing at least mildly plume-like Nd, Pb, and Sr isotopic characteristics (most abundant at ~17–17.5°S) and two slightly different high- $\epsilon_{\text{Nd}}$  mantle end-members equivalent to those north of 15.8°S and south of 20.7°S. Helium isotopes also define a prominent along-axis peak, but it spans a much narrower range of latitude and is offset slightly to the north of those for Nd, Sr and Pb isotopes. The combined results suggest that a discrete mantle heterogeneity may be entering into the melt zone near 15.8°S and migrating southward as far as the 20.7°S overlapping spreading center.

Isotopic variability at short length scales is very limited throughout the entire 13–23°S region. It cannot be solely a result of homogenization by petrogenetic processes, because there is a lack of corresponding uniformity in ratios of highly to moderately incompatible elements; also, isotopes do not correlate with major element indicators of degree of partial melting or differentiation, or, in general, with the secondary magmatic segmentation thought to reflect different partial melting domains. Therefore, the subaxial mantle must be isotopically well-mixed relative to the scale of melting. In part, this probably reflects: (1) a larger *volume* of melting per unit length of ridge; and (2) a greater flow of mantle into the subaxial melt zone at super-fast spreading; but also must represent (3) a reduced amount of real isotopic variability in the shallow asthenosphere, as emphasized by the regional isotopic uniformity north and south of the isotopic peak. Such large-scale homogeneity could be a result of enhanced convective asthenospheric

[CL]

mixing over a long period of time. It could also reflect a low, long-term input of continental, lithospheric, recycled slab, or plume-type material into the regional asthenosphere.

Largely independent of the north–south isotopic patterns is a fairly regular, southward depletion in highly incompatible elements such as Rb and Nb, superimposed on which is sizable local variability. Because ratios of highly to moderately incompatible elements show little or no correlation with major-element indicators of degree of melting, much of the variation in highly incompatible elements must be caused by a different (probably larger) volume of mantle than that conferring the major element signatures, or by one (or more) event that preceded the main melting episode in the not too ancient past.

## 1. Introduction

Isotopic ratios of Nd, Pb, and Sr in fresh mid-ocean ridge basalts (MORBs) are widely believed to reflect the composition of sources in the underlying convecting mantle, averaged at the scales of melting and melt mixing. The relationship of isotopic ratios to physical characteristics of ridges, such as spreading rate, segmentation, and axial bathymetry, is still unclear but, in contrast to several earlier studies, most recent workers have concluded that little or no correlation is present between spreading rate and either isotopic values or variances, at least in the Pacific [e.g., 1–3]. Holness and Richter [4], on the other hand, have suggested that this is true only for Pb isotopes and that a weak correlation of Nd and Sr isotopes, as well as La/Sm (and presumably other incompatible element) ratios, does exist with spreading rate if data for the Indian Ocean are excluded. However, their correlation is defined principally by data for slow and intermediate spreading rates (less than  $\sim 70$  mm/yr).

Few combined isotopic and trace element measurements are available for MORBs formed at so-called ‘super-fast’ spreading rates ( $> 130$  mm/yr), represented today by the East Pacific Rise both north and south of the Easter Microplate [5]. Previous isotopic results for several basalts from the 30–34.5°S section south of the microplate showed that Nd and Sr isotopes remain virtually constant, consistent with predictions of reduced isotopic variance at high spreading rates [1,6], but that Pb isotopic ratios increase in a southerly direction over a fairly wide range of values (e.g.,  $^{206}\text{Pb}/^{204}\text{Pb} = 18.59\text{--}18.91$ ) [3]. In contrast, data for several samples from 18.4–22.2°S, north of the microplate, showed what appeared to be a gentle north–south gradient in

Nd, Sr and Pb isotopic ratios [1,3]. Here, we discuss the results of a detailed isotopic and trace element investigation of a considerably longer section ( $\sim 1100$  km) of the ridge between 13°S and 23°S, carried out in conjunction with our recent major-element study [7].

In this area, the axis extends from the Pito Fracture Zone (the northern boundary of the Easter Microplate) to just north of the Garrett Fracture Zone (Fig. 1) and spreads at 150–160 mm/yr [e.g., 5]. Between these fracture zones are a number of ‘devals’ (deviations from axial linearity [8]) and several overlapping spreading centers (OSCs), including a major one at 20.7°S which appears to have been propagating southward for at least 3 m.y. [9]. The region is distant from hotspots; the closest being the mid-plate Easter or Sala y Gomez hotspot, which lies some 700–1100 km (depending on where the hotspot is located, exactly) southeast of the southernmost part of the study area. In addition to the physical segmentation of the ridge, along-axis major-element variations in basaltic glasses reveal a prominent compositional segmentation, termed secondary magmatic segmentation by Sinton et al. [7], which appears to correspond to the length scale of mantle melting variations; these workers defined 17 secondary magmatic segments with lengths between 11 and 185 km (Fig. 1).

## 2. Samples and methods

Most of the samples studied here were dredged on cruise 8712 of the University of Hawaii R.V. *Moana Wave* (labelled with MW prefix in Tables 1 and 2); several are from Scripps Institution of Oceanography’s 1983 Protea and 1981 Vulcan expeditions (PR and V prefixes), and four are

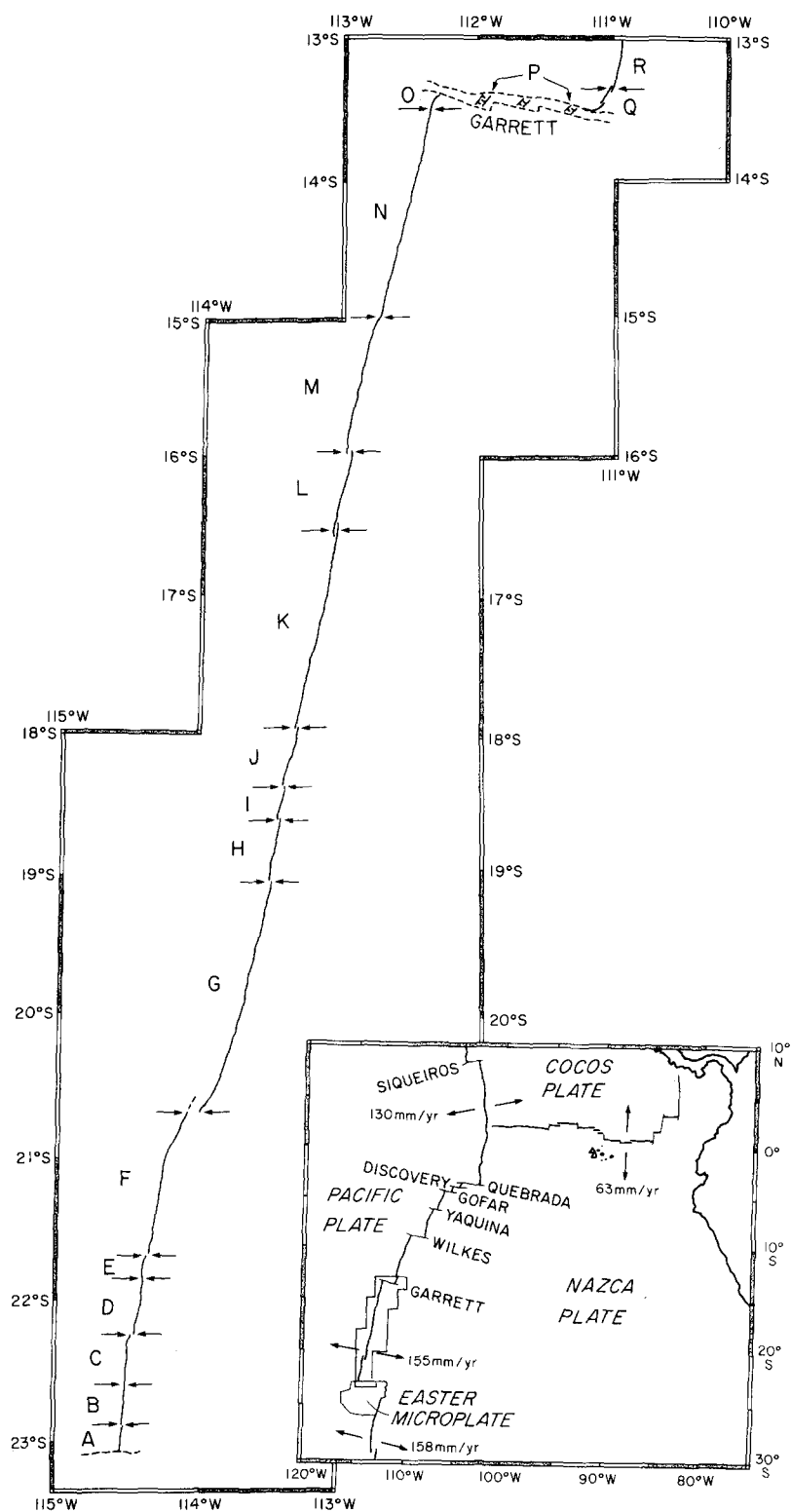


Fig. 1. Simplified map of the East Pacific Rise study area. Secondary magmatic segments defined on the basis of major elements [7] are indicated by A-R, and segment boundaries by arrows.

Table 1  
13–23°S East Pacific Rise isotopes

| Sample   | Seg. <sup>a</sup> | Latitude (°S) | εNd   | <sup>143</sup> Nd/ <sup>144</sup> Nd | <sup>87</sup> Sr/ <sup>86</sup> Sr | <sup>206</sup> Pb/ <sup>204</sup> Pb | <sup>207</sup> Pb/ <sup>204</sup> Pb | <sup>208</sup> Pb/ <sup>204</sup> Pb |
|----------|-------------------|---------------|-------|--------------------------------------|------------------------------------|--------------------------------------|--------------------------------------|--------------------------------------|
| MW104-2  | R                 | 13.08         | +10.6 | 0.513185                             | 0.70243                            | 18.113                               | 15.445                               | 37.622                               |
| MW103-4  | P,gfz             | 13.38         | +11.0 | 0.513206                             | 0.70248                            | 17.802                               | 15.430                               | 37.285                               |
| MW102-3  | O                 | 13.38         | +11.0 | 0.513202                             | 0.70241                            | 18.106                               | 15.441                               | 37.532                               |
| MW98-2   | n,T               | 13.80         | +10.7 | 0.513191                             | 0.70251                            | 18.173                               | 15.454                               | 37.669                               |
| MW96-1   | N                 | 14.10         | +10.7 | 0.513189                             | 0.70242                            | 18.141                               | 15.456                               | 37.589                               |
| MW93-1   | n,T               | 14.42         | +11.0 | 0.513202                             | 0.70250                            | 18.146                               | 15.444                               | 37.577                               |
| MW93-6   | N                 | 14.42         | +11.1 | 0.513211                             | 0.70241                            | 18.057                               | 15.433                               | 37.481                               |
| MW90-6   | n,T               | 14.85         | +10.5 | 0.513180                             | 0.70244                            | 18.263                               | 15.451                               | 37.685                               |
| MW87-3   | M                 | 15.17         | +10.8 | 0.513196                             | 0.70246                            | 18.107                               | 15.445                               | 37.571                               |
| MW84-2   | M                 | 15.52         | +11.0 | 0.513203                             | 0.70246                            | 18.108                               | 15.453                               | 37.593                               |
| MW82-4   | M                 | 15.83         | +10.8 | 0.513196                             | 0.70254                            | 18.098                               | 15.439                               | 37.556                               |
| MW80-6   | L                 | 16.05         | +10.1 | 0.513156                             | 0.70256                            | 18.289                               | 15.469                               | 37.786                               |
| MW77-1   | L                 | 16.57         | +9.9  | 0.513149                             | 0.70263                            | 18.417                               | 15.486                               | 37.931                               |
| MW75-2   | K                 | 16.75         | +9.3  | 0.513118                             | 0.70268                            | 18.562                               | 15.491                               | 38.053                               |
| CY84-7-4 | K                 | 17.00         | +8.9  | 0.513098                             | 0.70271                            |                                      |                                      |                                      |
| MW72-1   | K                 | 17.03         | +9.3  | 0.513118                             | 0.70269                            | 18.587                               | 15.493                               | 38.061                               |
| MW69-4   | K                 | 17.27         | +9.1  | 0.513105                             | 0.70269                            | 18.642                               | 15.501                               | 38.128                               |
| CY84-7-3 | k,T               | 17.43         | +9.2  | 0.513110                             | 0.70270                            |                                      |                                      |                                      |
| MW66-4   | K                 | 17.78         | +9.1  | 0.513104                             | 0.70266                            | 18.637                               | 15.505                               | 38.126                               |
| MW65-3   | J                 | 17.95         | +9.4  | 0.513122                             | 0.70265                            | 18.550                               | 15.507                               | 38.051                               |
| CY84-5-6 | I                 | 18.52         | +9.0  | 0.513103                             | 0.70261                            |                                      |                                      |                                      |
| MW61-1   | I                 | 18.60         | +9.4  | 0.513121                             | 0.70260                            | 18.514                               | 15.501                               | 38.033                               |
| PR1-8    | H                 | 18.85         | +9.8  | 0.513140                             | 0.70256                            |                                      |                                      |                                      |
| MW57-4   | H                 | 18.88         | +9.3  | 0.513115                             | 0.70263                            | 18.514                               | 15.490                               | 38.017                               |
| MW51-4   | H                 | 19.00         | +9.4  | 0.513122                             | 0.70262                            | 18.559                               | 15.507                               | 38.075                               |
| MW48-4   | g,T               | 19.30         | +9.4  | 0.513123                             |                                    | 18.541                               | 15.495                               | 38.029                               |
| PR-6A    | G,smt             | 19.54         | +9.2  | 0.513114                             | 0.70265                            |                                      |                                      |                                      |
| PR-6B    | G,smt             | 19.54         | +9.2  | 0.513111                             | 0.70261                            |                                      |                                      |                                      |
| PR-7     | G,smt             | 19.54         | +9.2  | 0.513111                             | 0.70260                            |                                      |                                      |                                      |
| MW43-3   | g,T               | 19.78         |       |                                      | 0.70265                            |                                      |                                      |                                      |
| MW41-1   | G                 | 19.92         | +9.8  | 0.513143                             | 0.70255                            | 18.464                               | 15.490                               | 37.960                               |
| CY84-4-1 | G                 | 20.17         | +9.9  | 0.513146                             | 0.70257                            |                                      |                                      |                                      |
| MW36-4   | G                 | 20.52         | +9.3  | 0.513119                             | 0.70261                            | 18.579                               | 15.517                               | 38.123                               |
| MW29-1   | F                 | 20.88         | +11.2 | 0.513215                             | 0.70237                            | 18.090                               | 15.456                               | 37.541                               |
| MW20-1   | F                 | 21.00         | +10.9 | 0.513199                             | 0.70241                            | 18.156                               | 15.466                               | 37.594                               |
| MW19-5   | F                 | 21.17         | +10.7 | 0.513188                             | 0.70241                            | 18.232                               | 15.480                               | 37.694                               |
| CY84-1-1 | F                 | 21.43         | +10.9 | 0.513198                             | 0.70241                            |                                      |                                      |                                      |
| MW15-3   | E                 | 21.80         | +10.5 | 0.513178                             | 0.70245                            | 18.239                               | 15.494                               | 37.703                               |
| MW10-2   | C                 | 22.35         |       |                                      | 0.70242                            |                                      |                                      |                                      |
| V8-1M    | C                 | 22.24         | +10.6 | 0.513183                             | 0.70240                            |                                      |                                      |                                      |
| MW9-5    | C                 | 22.48         | +11.0 | 0.513206                             | 0.70240                            | 18.068                               | 15.467                               | 37.529                               |
| MW8-12   | B                 | 22.74         |       |                                      | 0.70241                            |                                      |                                      |                                      |
| MW5-3    | A                 | 23.02         | +10.8 | 0.513193                             | 0.70239                            | 18.244                               | 15.476                               | 37.636                               |

from the 1984 collection of the French submersible *Cyana* (CY prefix). Excepting three lavas from near-ridge seamounts, all were taken at or very near the active spreading axis; Ra and Th isotopic data indicate that most of the MW samples are probably less than a few thousand years old [10]. This collection thus allows us to address spatial geochemical variations along-axis while minimizing complications arising from temporal variability. The majority of lavas recovered are moderately evolved, incompatible-element-depleted normal (or N-) MORBs, but a number of transitional (or T-) MORBs, characterized by enrichment in K (and other highly incompatible elements) relative to Ti or P (and other moderately incompatible elements), are also present, and a near-continuum exists between extreme compositions [7]. Here we define as T-MORBs any samples with  $Rb > 2$  ppm and  $Rb/Nd > 0.15$ .

All isotopic and isotope dilution determinations were made on fresh, generally phenocryst-free chips of handpicked glass; all but six of the analyses here are of N-MORBs. Nd, Pb and Sr isotopes were measured for the MW samples at the University of Hawaii following [11]; the remaining samples were analyzed for Sr and Nd isotopes at Scripps Institution after [1]; the isotopic data appear in Table 1. For the MW samples, Nb, K, Sr, P, Zr, Y, Ti, Sc, V, Co, Cr and Ni abundances were determined (in duplicate) at the University of Hawaii on alumina-ground whole-rock powders following [12], and using a Siemens 303AS X-ray fluorescence spectrometer with a Rh X-ray tube. For the PR, V and CY samples, K, P and Ti were determined on glasses by conventional electron microprobe methods at Scripps. The results are given in Table 2, along with

isotope dilution measurements for Nd, Sm, Sr, Rb and Pb. Although the whole rocks analyzed by X-ray fluorescence were very fresh and generally nearly aphyric, they were not strictly identical to the glass separates used for isotope dilution; nevertheless, the whole-rock and glass values for Sr (the only element analyzed by both methods) are generally in close agreement. Helium isotopes have been also measured on splits of a subset of the glasses; the data and analytical methods are reported by Kurz et al. [53].

### 3. Results

#### 3.1. Isotopes

Nd, Pb and Sr isotopic ratios display remarkably smooth and regular patterns when plotted against latitude (Fig. 2a–c). The patterns are closely similar in shape, the key feature being a broad region of elevated  $^{87}Sr/^{86}Sr$  (up to 0.70271),  $^{206}Pb/^{204}Pb$  (to 18.64), and lower  $\epsilon_{Nd}$  (to +8.9), reaching a peak around 17.0–17.5°S. North of 17°S, values fall away smoothly to about 15.8°S; between 15.8°S and 13.08°S, with one exception (see below), they vary only slightly:  $\epsilon_{Nd} = +10.5$  to +11.1,  $^{87}Sr/^{86}Sr = 0.70241$ –0.70254, and  $^{206}Pb/^{204}Pb = 18.06$ –18.17, with one sample at 18.26. South of about 17.5°S there is a much more gradual isotopic gradient, which terminates at the large 20.7°S OSC. Farther south, from 20.7° to 23°S, values are again quite constant ( $^{87}Sr/^{86}Sr = 0.70237$ –0.70245,  $\epsilon_{Nd} = +10.5$  to +11.2,  $^{206}Pb/^{204}Pb = 18.07$ –18.24) and similar to those from 13.1° to 15.8°S. They are not identical, however, for the southern group possesses slightly but

#### Notes to Table 1:

<sup>a</sup> Seg. = Secondary magmatic segment of Sinton et al. [7]. T = T-MORB, smt = off-axis seamount, gFz = Garrett Fracture Zone. Isotopic fractionation corrections are  $^{148}NdO/^{144}NdO = 0.242436$  ( $^{148}Nd/^{144}Nd = 0.241572$ ),  $^{86}Sr/^{88}Sr = 0.1194$ ; Pb isotopic ratios are corrected for fractionation using the NBS 981 Pb standard values of Todt et al. [51]. Nd and Sr data are reported relative to University of Hawaii values for La Jolla Nd (0.511855) and NBS 987 Sr (0.71024) standards. Uncertainties on Nd and Sr isotopic data are less than or equal to the maximum external errors on these standards (for multicollector data:  $\pm 0.000012$  (0.2  $\epsilon$  units) for La Jolla Nd and  $\pm 0.000022$  for NBS 987 Sr; for single collector data:  $\pm 0.000014$  (0.3  $\epsilon$  units) and  $\pm 0.000026$ , respectively). Uncertainties on Pb isotopes are less than  $\pm 0.012$  for  $^{206}Pb/^{204}Pb$ ,  $\pm 0.012$  for  $^{207}Pb/^{204}Pb$ , and  $\pm 0.038$  for  $^{208}Pb/^{204}Pb$ . Total procedural blanks are negligible: 5–40 pg for Pb, < 20 picograms for Nd, < 120 pg for Sr. Note that  $\epsilon_{Nd} = 0$  corresponds to  $^{143}Nd/^{144}Nd = 0.512640$ .

Table 2  
13–23°S East Pacific Rise trace elements (in ppm)

| Sample   | Rb   | K     | Nb   | Pb    | Sr    | SrXRF <sup>a</sup> | Nd    |
|----------|------|-------|------|-------|-------|--------------------|-------|
| MW104-2  | 1.04 | 920   | 2.4  | 0.287 | 107.0 | 109                | 7.831 |
| MW103-4  | 0.05 | 170   | 0.6  | 0.108 | 71.00 | 69                 | 4.108 |
| MW102-3  | 1.21 | 1000  | 3.2  | 0.389 | 103.8 | 104                | 11.54 |
| MW98-2   | 2.06 | 1580  | 4.9  | 0.377 | 122.5 | 133                | 9.502 |
| MW96-1   | 1.17 | 830   |      | 0.372 | 121.6 |                    | 10.69 |
| MW93-1   | 5.01 | 2830  | 9.8  | 0.954 | 121.3 | 121                | 31.79 |
| MW93-6   | 0.84 | 670   | 2.7  | 0.296 | 99.40 | 100                | 8.524 |
| MW90-6   | 2.52 | 1580  | 6.1  | 0.464 | 106.5 | 130                | 12.56 |
| MW87-3   | 1.20 | 1080  | 3.6  | 0.454 | 97.90 | 100                | 12.55 |
| MW84-2   | 1.19 | 1000  | 3.6  | 0.436 | 100.9 | 95                 | 13.23 |
| MW82-4   | 1.30 | 670   | 3.9  | 0.448 | 113.9 | 99                 | 14.06 |
| MW80-6   | 0.67 | 670   | 2.5  | 0.338 | 93.67 | 90                 | 10.90 |
| MW77-1   | 0.65 | 750   | 2.5  |       | 93.33 | 90                 | 10.23 |
| MW75-2   | 0.57 | 830   | 2.5  | 0.294 | 93.17 | 101                | 9.024 |
| CY84-7-4 | 0.98 | 920   |      |       | 110.5 |                    | 10.36 |
| MW72-1   | 1.01 | 920   | 2.8  | 0.314 | 90.12 | 101                | 9.522 |
| MW69-4   | 0.92 | 750   | 3.0  | 0.254 | 104.4 | 108                | 7.70  |
| CY84-7-3 | 2.02 | 1830  |      |       | 130.0 |                    | 12.46 |
| MW66-4   | 0.44 | 500   | 1.9  | 0.342 | 96.63 | 95                 | 9.195 |
| MW65-3   | 0.40 | 420   | 2.3  | 0.271 | 96.37 | 98                 | 8.192 |
| CY84-5-6 | 1.15 | 1830  |      |       | 130.1 |                    | 11.71 |
| MW61-1   | 0.56 | 1000  | 2.8  | 0.438 | 122.7 | 117                | 12.43 |
| PR1-8    | 1.01 | 1080  |      |       | 99.31 |                    | 13.16 |
| MW57-4   | 0.48 | 500   | 3.1  | 0.370 | 114.7 | 119                | 10.17 |
| MW51-4   | 0.41 | 580   | 1.7  | 0.283 | 97.04 | 94                 | 8.493 |
| MW48-4   | 3.49 | 1330  | 6.0  | 0.369 |       | 112                | 10.33 |
| PR-6A    | 1.13 | 920   |      |       | 109.5 |                    | 10.69 |
| PR-6B    | 1.62 | 1330  |      |       | 114.9 |                    | 14.98 |
| PR-7     | 0.75 | 920   |      |       | 109.4 |                    | 11.07 |
| MW43-3   | 4.75 | 2500  | 10.6 |       | 142.3 | 136                |       |
| MW41-1   | 0.68 | 920   | 3.7  | 0.496 | 93.21 | 89                 | 16.61 |
| CY84-4-1 | 1.14 | 1080  |      |       | 93.75 |                    | 17.01 |
| MW36-4   | 1.98 | 1250  | 5.2  | 0.550 | 99.67 | 94                 | 17.67 |
| MW29-1   | 0.23 | 580   | 1.9  | 0.258 | 98.42 | 104                | 7.188 |
| MW20-1   | 0.22 | 580   | 1.6  | 0.320 | 97.80 | 105                | 8.505 |
| MW19-5   | 0.33 | 500   | 1.6  | 0.326 | 77.35 | 82                 | 9.087 |
| CY84-1-1 | 0.63 | 750   |      |       | 116.6 |                    | 9.720 |
| MW15-3   | 0.51 | 500   | 2.6  | 0.370 | 81.68 | 78                 | 12.05 |
| MW10-2   | 0.49 | 500   | 2.8  |       | 105.6 | 104                |       |
| V8-1M    | 0.46 | 580   |      |       | 104.2 |                    | 9.700 |
| MW9-5    | 0.50 | 580   | 2.8  | 0.378 | 119.7 | 118                | 11.42 |
| MW8-12   | 0.27 | 330   | 1.3  |       | 81.10 | 87                 |       |
| MW5-3    | 0.10 | 250   | 1.1  | 0.156 | 75.39 | 69                 | 5.983 |
| BCR-1    |      |       |      |       |       |                    |       |
| meas.    | 46.2 | 14280 | 12.3 | 13.53 | 329.4 | 328                | 28.51 |
| rec.     | 46.8 | 14110 | 14   | 13.6  | 330   | 330                | 28.8  |

Table 2 (continued). For notes, see next page

| P    | Zr  | Sm    | Ti    | Y   | Sc | V   | Co | Cr  | Ni  |
|------|-----|-------|-------|-----|----|-----|----|-----|-----|
| 524  | 80  | 2.805 | 7860  | 30  |    | 301 | 47 | 347 | 102 |
| 180  | 39  | 1.801 | 4980  | 25  | 35 | 202 | 61 | 595 | 346 |
| 660  | 118 | 4.109 | 10800 | 45  | 44 | 403 | 45 | 86  | 54  |
| 660  | 105 | 3.186 | 9420  | 35  | 40 | 321 | 43 | 295 | 95  |
|      |     | 3.656 | 10320 |     |    |     |    |     |     |
| 2020 | 346 | 10.43 | 11100 | 100 | 39 | 241 | 34 | 161 | 52  |
| 530  | 87  | 3.095 | 8880  | 35  | 47 | 352 | 48 | 234 | 86  |
| 840  | 135 | 4.201 | 11760 | 45  | 44 | 390 | 46 | 63  | 52  |
| 840  | 142 | 4.457 | 12720 | 52  | 47 | 440 | 44 | 201 | 66  |
| 792  | 136 | 4.730 | 12600 | 51  | 49 | 456 | 45 | 206 | 70  |
| 873  | 151 | 5.010 | 11040 | 53  |    | 465 | 44 | 158 | 70  |
| 620  | 108 | 4.023 | 10680 | 43  | 45 | 401 | 45 | 229 | 81  |
| 620  | 103 | 3.770 | 10200 | 41  | 46 | 399 | 48 | 255 | 81  |
| 570  | 102 | 3.302 | 10140 | 40  | 46 | 386 | 46 | 187 | 72  |
| 570  |     | 3.660 | 10680 |     |    |     |    |     |     |
| 660  | 112 | 3.468 | 10860 | 43  | 48 | 406 | 47 | 140 | 60  |
| 480  | 81  | 2.738 | 8040  | 31  | 44 | 319 | 46 | 391 | 132 |
| 880  |     | 4.170 | 12300 |     |    |     |    |     |     |
| 570  | 93  | 3.423 | 9780  | 37  |    | 363 | 46 | 239 | 95  |
| 440  | 86  | 3.064 | 8820  | 36  | 49 | 344 | 47 | 225 | 86  |
| 970  |     | 4.000 | 12240 |     |    |     |    |     |     |
| 620  | 123 | 4.408 | 11340 | 43  | 50 | 389 | 59 | 50  | 44  |
| 840  |     | 4.650 | 12420 |     |    |     |    |     |     |
| 620  | 115 | 3.581 | 10140 | 40  | 45 | 322 | 45 | 340 | 137 |
| 400  | 84  | 3.175 | 8520  | 33  | 48 | 354 | 43 | 223 | 68  |
| 880  | 153 | 3.490 | 12960 | 51  | 50 | 448 | 42 | 54  | 51  |
| 620  |     | 3.750 | 10380 |     |    |     |    |     |     |
| 1140 |     | 4.960 | 13320 |     |    |     |    |     |     |
| 700  |     | 3.900 | 10740 |     |    |     |    |     |     |
| 920  | 143 |       | 11700 | 43  | 43 | 381 | 43 | 278 | 88  |
| 920  | 167 | 5.912 | 14880 | 61  | 48 | 485 | 40 | 96  | 57  |
| 790  |     | 6.020 | 14760 |     |    |     |    |     |     |
| 1010 | 178 | 6.213 | 15540 | 63  | 47 | 510 | 44 | 60  | 42  |
| 440  | 82  | 2.560 | 7500  | 30  | 41 | 270 | 41 | 365 | 122 |
| 530  | 92  | 3.076 | 8220  | 34  | 49 | 309 | 40 | 344 | 79  |
| 620  | 104 | 3.437 | 10560 | 43  | 46 | 398 | 45 | 182 | 69  |
| 620  |     | 3.420 | 9120  |     |    |     |    |     |     |
| 1060 | 121 | 4.607 | 12180 | 51  | 48 | 434 | 47 | 88  | 56  |
| 660  | 117 |       | 10560 | 43  | 47 | 364 | 42 | 317 | 90  |
| 620  |     | 3.510 | 9360  |     |    |     |    |     |     |
| 480  | 118 | 4.035 | 10620 | 37  | 42 | 342 | 43 | 323 | 91  |
| 400  | 73  |       | 7680  | 32  |    | 330 | 44 | 266 | 78  |
| 350  | 54  | 2.411 | 6120  | 28  | 45 | 291 | 44 | 364 | 105 |
|      |     |       |       |     |    |     |    |     |     |
| 1670 | 193 | 6.576 | 13440 | 38  | 30 | 405 | 35 | 15  | 11  |
| 1584 | 190 | 6.60  | 13500 | 38  | 33 | 407 | 37 | 16  | 13  |

consistently higher  $^{207}\text{Pb}/^{204}\text{Pb}$  for a given  $^{206}\text{Pb}/^{204}\text{Pb}$  (Fig. 3a), and slightly lesser  $^{87}\text{Sr}/^{86}\text{Sr}$  (Figs. 4 and 5), on average, than the 13.1–15.8°S group.

Note that the total range of isotopic variation in both the 13.1–15.8°S and 20.7–23°S areas—that is, over distances of more than 300 and 250 km, respectively—is not significantly greater than the small-scale variation (i.e., that at a given latitude or, rather, over a small span of latitude). In turn, the small-scale variation is surprisingly limited throughout the study area, essentially within analytical errors for Nd and, in most places, within or only slightly greater than analytical uncertainty for Sr isotopes. This result is strongly reminiscent of the 30–34.5°S region, with the critical difference that here Pb isotopes behave very much like Sr and Nd isotopes (see below).

Very little correspondence exists between isotopic ratios and axial bathymetry, or the small OSCs and devals that physically segment the rise in this area. The second largest OSC in the region, at 15.9°S, roughly coincides with the foot of the north flank of the isotopic peak in Fig. 2a–c, but the regular, regional isotopic pattern is disturbed markedly in only two places: at the 20.7°S OSC, and in the Garrett Fracture Zone. The 20.7°S OSC marks a clear discontinuity in all three isotopic systems, and the differences across it appear slightly amplified closest to the offset; the highest  $\epsilon_{\text{Nd}}$  and lowest  $^{87}\text{Sr}/^{86}\text{Sr}$  of the entire study area occur immediately to the south of the offset (sample MW29-1), whereas the lava from just to the north (MW36-1) displays somewhat higher  $^{87}\text{Sr}/^{86}\text{Sr}$ ,  $^{206}\text{Pb}/^{204}\text{Pb}$  and lower  $\epsilon_{\text{Nd}}$  than its nearby neighbors. Note that this situation is not a “transform fault effect” [13], because the slightly incompatible-element-enriched MW36-1

does not appear to represent a particularly low degree of melting (as estimated from major elements; e.g., following [14]), whereas MW29-1 does represent a local minimum in degree of melting, but has low  $^{87}\text{Sr}/^{86}\text{Sr}$  and is depleted in incompatible elements (Table 2). We suspect these characteristics are related to the southward propagation of the axis north of the offset and the failure of spreading on the southern side of the offset [7; cf. 15].

In contrast to the 20.7°S OSC, no obvious isotopic offset is evident across the Garrett Fracture Zone but, within it, a small pull-apart basin in the transform fault zone yielded a sample (MW103-4) with much lower Pb isotope ratios ( $^{206}\text{Pb}/^{204}\text{Pb} = 17.80$ ) than any others we have analyzed, and among the lowest yet measured for Pacific MORB [cf. 16]. Its Nd and Sr isotopic values, however, are indistinguishable from those of the 13.1–15.8°S axial lavas; chemically, samples from this dredge haul are the most depleted in incompatible elements of any in our collection and are among the most depleted yet reported for MORB (e.g., for MW103-4: Rb = 0.05 ppm, Nb = 0.6 ppm and Pb = 0.108 ppm).

Putting the above results in perspective, the total spread of isotopic values from 13°S to 23°S is modest, comparable to that of previously published data for the East Pacific Rise as a whole, if the Easter Microplate is excluded. All of the values, even those at the isotopic peak, are within the global range of normal MORB. Overall, however, the correlations between isotopic ratios are significantly better than for the East Pacific Rise as a whole (e.g., Fig. 4). That for  $^{208}\text{Pb}/^{204}\text{Pb}$  versus  $^{206}\text{Pb}/^{204}\text{Pb}$  is nearly perfect, despite the fact that  $^{207}\text{Pb}/^{204}\text{Pb}$  values for the 13.1–15.8°S and 20.7–23°S groups are subtly but distinctly

#### Notes to Table 2:

<sup>a</sup> SrXRF = Sr determined by X-ray fluorescence.

Isotope-dilution measurements of Rb, Pb, Sr, Nd, and Sm have relative uncertainties of ~1%, <1%, <0.5%, <0.2% and <0.2%, respectively. Absolute uncertainties on X-ray fluorescence data are about 80 ppm for K, 0.3 ppm for Nb, 1 ppm for Sr, 45 ppm for P, 5 ppm for Zr, 60 ppm for Ti, 1 ppm for Y, 2 ppm for Sc, 3 ppm for V, 3 ppm for Cr, 2 ppm for Co, and 2 ppm for Ni. Microprobe measurements of K, Ti, and P in PR, V, and CY samples have relative uncertainties of 5–10%. Note that X-ray fluorescence data were collected on whole-rock powders rather than glass separates identical to those analyzed by isotope dilution. An indication of accuracy is given by measured ( $n = 50$  for K, P, Ti;  $n = 11$  for other elements measured by X-ray fluorescence;  $n = 2$  for elements measured by isotope dilution) and recommended [52] values for standard rock BCR-1.



different (Fig. 3). The 13.1–15.8°S and 20.7–23°S samples also cannot be distinguished in the good correlation on the  $^{206}\text{Pb}/^{204}\text{Pb}$  against  $\epsilon_{\text{Nd}}$  diagram (Fig. 5a), but can be differentiated on the other plots in Figs. 4 and 5 because of the lesser  $^{207}\text{Pb}/^{204}\text{Pb}$  and slightly greater  $^{87}\text{Sr}/^{86}\text{Sr}$  of the former group.

Helium isotopic data are discussed in detail by Kurz et al. [53]. Briefly, the latitudinal pattern for He (Fig. 2d) displays significant differences from those for the other isotopes. Although a pronounced peak is present in  $^3\text{He}/^4\text{He}$ , reaching a maximum  $R/R_{\text{atm}}$  of 11.0 (where  $R/R_{\text{atm}} = ^3\text{He}/^4\text{He}$  of a sample  $\div ^3\text{He}/^4\text{He}$  of the Earth's atmosphere), it is: (1) much narrower than those for the other isotopes; (2) its maximum point appears to be offset slightly to the north, by at least 30–50 km; and (3) no discontinuity exists in He isotope ratios across the 20.7°S OSC. Indeed, south of about 18.5°S,  $R/R_{\text{atm}}$  lies between 8.0 and 8.5, well within the normal MORB range [e.g., 17–21]. North of  $\sim 15.8^\circ\text{S}$  it is somewhat greater, between 8.7 and 9.2, and the unusual, highly incompatible-element-depleted Garrett Fracture Zone sample MW103-4 has an even higher value of 9.7. Also, in contrast to the other isotopic ratios,  $R/R_{\text{atm}}$  at the peak is well above normal values for MORBs, approaching those of some high- $^3\text{He}/^4\text{He}$  oceanic island (hotspot) volcanoes [e.g., 12,17,19,23].

### 3.2. Incompatible trace elements

Surprisingly, the smooth, peaked isotopic patterns of Fig. 2 are *not* mirrored by latitudinal variations in incompatible trace elements or inter-element ratios (Fig. 6). Nor do incompatible element ratios show much correlation with isotopic ratios (e.g., Fig. 7); removing the T-MORB samples from consideration generally leads to little or no improvement. This very poor overall correspondence between isotopic and incompatible element ratios constitutes an important difference between the 13–23°S area and several other well-studied sections of the world's ridge system. The latter regions differ fundamentally from the present area in that they appear to be the sites of interaction between the spreading

axis and long-lived, near-ridge hotspots [e.g., 24–26].

Although distinct from the isotopic patterns, incompatible element ratios at 13–23°S do show systematic behavior with latitude. In particular, there is an overall northward increase in highly incompatible element to moderately incompatible element ratios (e.g., Fig. 6a,b), as also noted by Sinton et al. [7] for K, Ti and P. The Rb/Nd ratio, for instance, can vary considerably over a small range of latitude (especially if the T-MORB samples are included), but with the exception of the highly depleted Garrett Fracture Zone sample MW103-4, the *minimum* Rb/Nd value observed increases northward rather steadily by a factor of about seven. In agreement with Rb being more incompatible than K or Nb [e.g., 27], ratios of K and Nb to Nd, Zr, Sm, etc., show more modest northward increases, as well as less variation at a given latitude. Gentler (or no) latitudinal gradients are seen for ratios of elements that have more similar incompatibilities (e.g., Sm/Nd, Zr/Nd, Ti/Y; see Fig. 6d), and little or no difference is evident between N-MORBs and T-MORBs in such ratios. Primitive-mantle-normalized incompatible element patterns (Fig. 8f) confirm that the enrichment of the T-MORBs is mainly confined to the highly incompatible elements.

Whatever the ultimate cause of the observed variations, ratios made up of two incompatible elements known to have different solid–melt partitioning characteristics generally correlate well with one another on bivariate plots, and in a manner consistent with the relative order of incompatibility commonly believed to be obtained for MORB mantle [e.g., 27]. This behavior is useful because it allows estimation of the relative incompatibility of elements whose partitioning characteristics are poorly known or even controversial. Pb is one such element, partly because high quality Pb abundance data are limited for samples well characterized for other elements. Our results show that at 13–23°S Pb behaves very similarly to Nd or Zr; that is, it appears less incompatible than Rb, K, or Nb, but more incompatible than, say, Y (e.g., Fig. 8a,c–e). Unlike Rb/Nd or Nb/Zr, for example, Pb/Zr and Pb/

Nd vary little with latitude, or at a given latitude, and there is essentially no difference between N-MORB and T-MORB values (Fig. 6c). Our results, therefore, argue against the notion that Pb is effectively more incompatible than Nb, U,

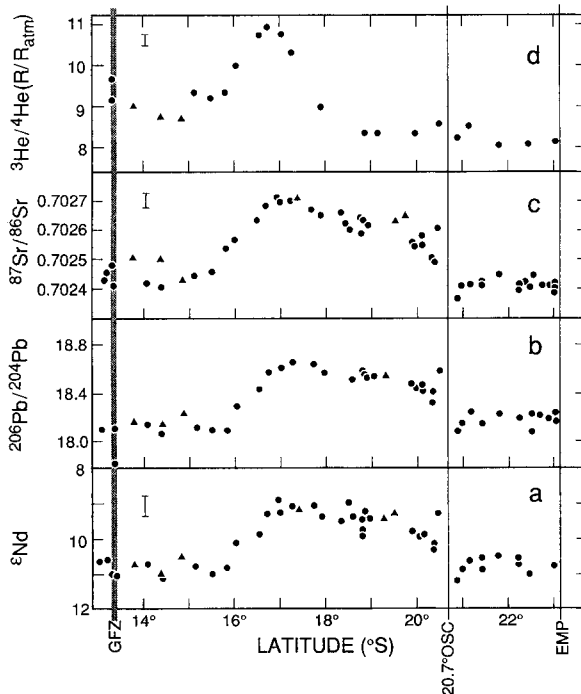


Fig. 2. Isotopic variations versus latitude for axial lavas: (a)  $\epsilon_{\text{Nd}}$ , (b)  $^{206}\text{Pb}/^{204}\text{Pb}$ , (c)  $^{87}\text{Sr}/^{86}\text{Sr}$  and (d)  $^3\text{He}/^4\text{He}$  as  $\text{R}/\text{R}_{\text{atm}}$  [He data from 53]. Note that the scale for  $\epsilon_{\text{Nd}}$  increases downward, so that the shape of the Nd isotope pattern can be compared directly with those for the other isotopes. Dots = N-MORBs; triangles = T-MORBs; vertical lines running through all panels = latitudes of the Garrett Fracture Zone (GFZ), 20.7°S OSC, and northern boundary of the Easter Microplate (EMP). In addition to our results, high-quality data (omitting only one Sr and one Pb isotope measurement) are shown from studies by Macdougall and Lugmair [1], White et al. [3], Hanan and Schilling [16] and Fontignie and Schilling [26]. Data for several samples from yet earlier studies are not used, as most of the measurements lie substantially above or below the trends defined by all the other data and, in the case of Pb, are often anomalously low or high in  $^{207}\text{Pb}/^{204}\text{Pb}$ , suggesting experimental problems during analysis. Error bars for Nd and Sr isotopes are for data in this study; analytical errors for  $^{206}\text{Pb}/^{204}\text{Pb}$  are smaller than the data points. Error bar in He isotope panel represents a typical uncertainty for the data of Kurz et al. [53].

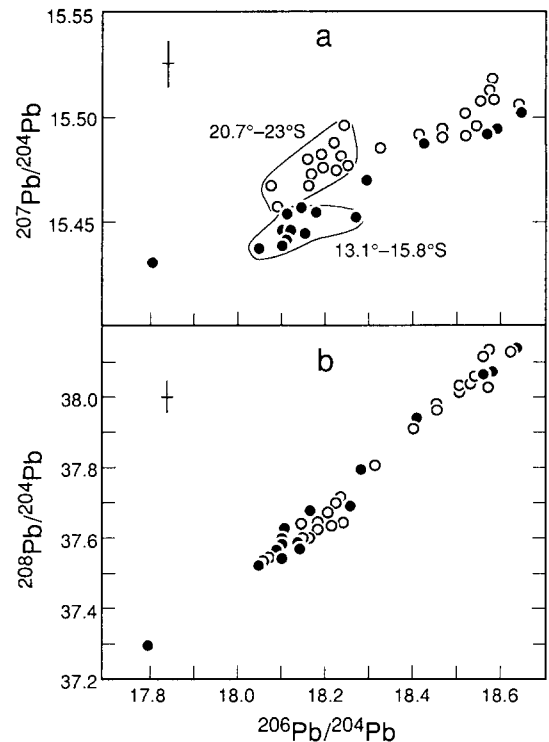


Fig. 3. (a)  $^{207}\text{Pb}/^{204}\text{Pb}$  vs.  $^{206}\text{Pb}/^{204}\text{Pb}$  and (b)  $^{208}\text{Pb}/^{204}\text{Pb}$  vs.  $^{206}\text{Pb}/^{204}\text{Pb}$  for the data shown in Fig. 2. Circles and dots = results for samples from south and north of 17.3°S, respectively. Fields are delineated in (a) for the 20.7–23°S and 13.1–15.8°S groups. Error bars are for data in this study.

or even Rb [e.g., 28–30]—at least in the modern MORB mantle—but are in general agreement with the suggestion that Pb behaves rather similarly to Ce [e.g., 31,32] (however, based on our still limited Ce data [J. Sinton, unpubl.], Ce/Nd, Ce/Zr, and Ce/Pb show more variation than Pb/Nd or Pb/Zr, apparently implying an effective incompatibility for Pb closer to that of Nd than Ce). Note that this conclusion holds regardless of what specific mechanisms control the behavior of Pb in the MORB source, such as solid–melt equilibrium ionic partitioning, diffusion, etc., because Pb elemental abundances in the lavas reflect the integrated record of all processes causing inter-element differentiation prior to eruption (and Pb remains incompatible during MORB magmatic differentiation).

### 3.3. Relationship of isotopes and trace elements to major element melting parameters

Neither isotopic nor incompatible element ratios of the samples listed in Tables 1 and 2 correlate with major element indicators of degree or depth of melting, such as fractionation-corrected total FeO or Na<sub>2</sub>O [e.g., 33]; this is true whether using fractionation-corrected oxide values for individual samples or the mean values for secondary magmatic segments (Fig. 9). Similarly, there is no correlation with the percentage of melting as estimated from major element parameters by the method of Niu and Batiza [14]. Also, no correspondence exists between isotopic ratios and the seventeen secondary magmatic segments defined by major elements, with the exception of the 20.7°S OSC and, possibly, a magmatic segment boundary coinciding with the 15.9°S OSC, situated near the base of the north flank of the isotopic peak. Because the secondary magmatic segmentation largely appears to reflect different partial melting domains [7], these results indicate that variations in partial melting producing the major element differences are not generally cou-

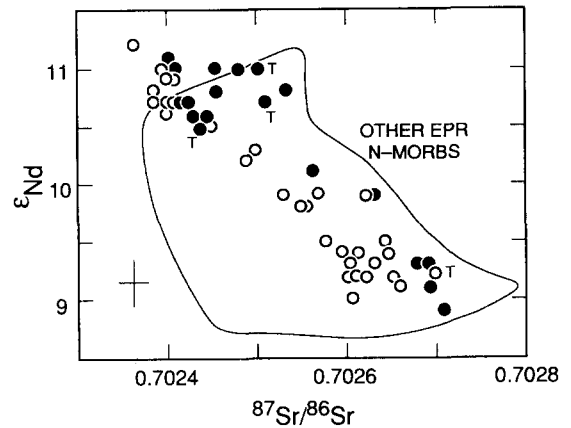


Fig. 4.  $\epsilon_{\text{Nd}}$  vs.  $^{87}\text{Sr}/^{86}\text{Sr}$ . Symbols as in Fig. 3. Note that  $^{87}\text{Sr}/^{86}\text{Sr}$  tends to be slightly greater for lavas from the northern part of the study area. Points labelled with a 'T' represent T-MORBs. Field for other EPR N-MORBs (excluding the Easter Microplate) is from the data of Macdougall and Lugmair [1], White et al. [3] and references therein. Error bar is for data in this study.

pled to, nor the cause of, the Nd, Pb, or Sr isotopic patterns. These isotopic patterns must, therefore, primarily represent patterns extant in the mantle source prior to melting.

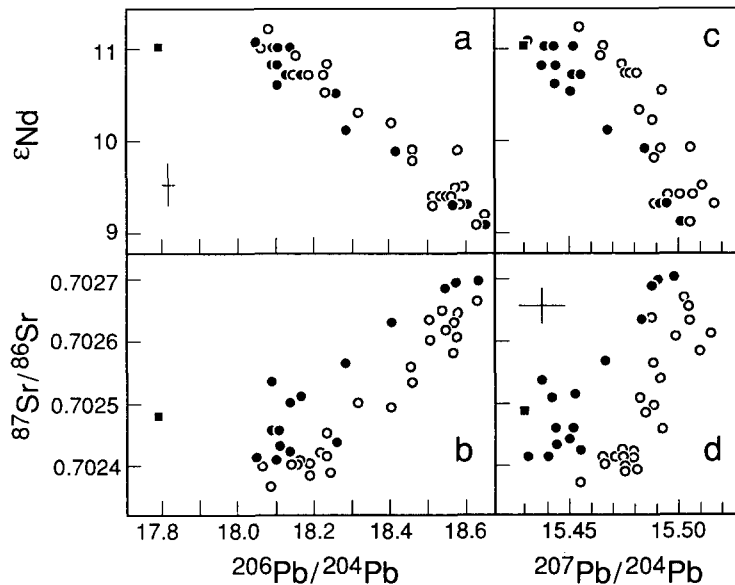


Fig. 5. Plots of  $\epsilon_{\text{Nd}}$  and  $^{87}\text{Sr}/^{86}\text{Sr}$  vs.  $^{206}\text{Pb}/^{204}\text{Pb}$  (a and b) and  $^{207}\text{Pb}/^{204}\text{Pb}$  (c and d). Symbols as in Figs. 3 and 4, except that the square point falling far from the main data array in (a) and (b) is for Garrett Fracture Zone sample MW103-4.

Another important conclusion is that much of the variation in highly incompatible elements, particularly their general, regional southward depletion, must not be produced by the same volume of mantle or perhaps even in the same melting episode(s) responsible for the fractionation-adjusted major element variations. (Indeed, the secondary magmatic segments north of 17°S may correspond to slightly *greater* average degrees of melting than the southern segments—e.g., see top right panel in Fig. 9). However, because the incompatible element and isotopic ratios behave more or less independently of one another, much of the observed incompatible element variation must reflect processes that are relatively recent compared to the time scales of isotopic evolution. For instance, the biggest differences in incompatible element ratios occur between the T- and N-MORBs, but the several T-MORBs analyzed here have Nd isotopic values identical (within errors) to those of adjacent N-MORBs. No systematic difference is apparent between N- and T-MORBs in Pb isotopes, either,

although one of the three T-MORBs from the 13.1–15.8°S group has somewhat higher  $^{206}\text{Pb}/^{204}\text{Pb}$  (MW90-6 at 18.26 as opposed to 18.14–18.06 for the N-MORBs). In the one case where a T- and N-MORB from the same dredge haul were analyzed (MW93-1 and -6), the T-MORB displays higher  $^{206}\text{Pb}/^{204}\text{Pb}$ , but only by 0.09 (18.15 and 18.06, respectively). Sr isotope ratios for two of the T-MORBs are indistinguishable from those of nearby N-MORBs, but are slightly higher for the other four; the maximum difference of only 0.00009 occurs between samples MW93-1 and MW93-6 from the same dredge haul. If interpreted in terms of an age of local Rb enrichment in the source of the T-MORB (assuming, simplistically, that the  $^{87}\text{Rb}/^{86}\text{Sr}$  ratios in the two samples represent those in their sources), a value of  $\sim 80$  m.y. is obtained. Although we have not measured U or Th, only a modest, and quite plausible, difference of  $\sim 7$  in the  $^{238}\text{U}/^{204}\text{Pb}$  and  $\sim 24$  in the  $^{232}\text{Th}/^{204}\text{Pb}$  values of the N- and T-MORB sources would be required to obtain the observed difference in Pb

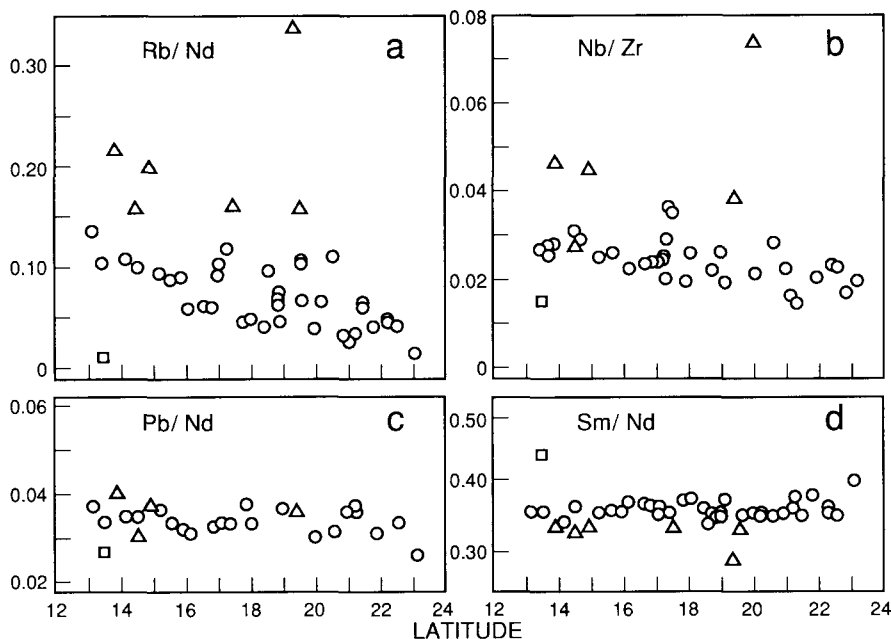


Fig. 6. Latitudinal variation of representative incompatible element ratios (using data from Table 2 and Macdougall and Lugmair, unpublished). Triangle = T-MORB; square = sample MW103-4.

isotope ratios by radiogenic ingrowth in 80 m.y. For some of the other T-MORBs, the enrichment could be much more recent.

#### 4. Discussion and conclusions

##### 4.1. Small-scale homogeneity

Processes of partial melting, melt migration, and magmatic differentiation are generally thought to have little direct effect on isotopic ratios, although it has been suggested that melt migration or disequilibrium melting might decouple inter-element isotopic ratios under some conditions [e.g., 10,29,30,34]. At 13–23°S, the close overall correspondence of Pb, Nd and Sr isotopes demonstrates that this is not a significant concern for these three elements. Also, because the strik-

ing homogeneity of isotopic values, both over small spans of latitude and regionally at 13.1–15.8°S and 20.7–23°S, is unaccompanied by similar uniformity in ratios of Rb/Nd, etc. (e.g., Fig. 6a), it appears that isotopic homogeneity is not a product solely of melting, melt migration or extraction processes. The idea that more efficient mixing of magmas in axial magma chambers could damp the isotopic variance at fast spreading rates [e.g., 35], questionable in light of recent advances in understanding such chambers [e.g., 36], is ruled out at 13–23°S by the lack of correlation between our isotopic and major element (or trace element) data (e.g., Fig. 7a). For example, lavas with  $\epsilon_{\text{Nd}} \sim +9.2$  cover virtually the entire range of MgO/FeO\*. Instead, the most straightforward interpretation is that the isotopic composition of the mantle feeding short sections of the ridge must be quite uniform to a scale less than that of

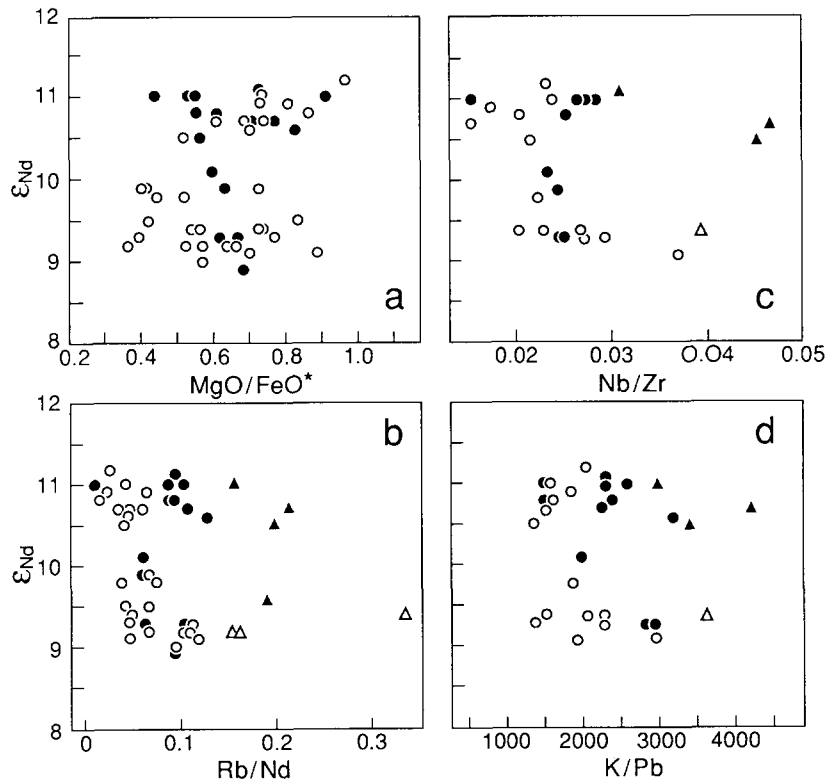


Fig. 7.  $\epsilon_{\text{Nd}}$  vs. (a) MgO/FeO\* (FeO\* = total iron as FeO), (b) Rb/Nd, (c) Nb/Zr and (d) K/Pb. Symbols as in Fig. 5, except that T-MORBs are indicated by triangles.

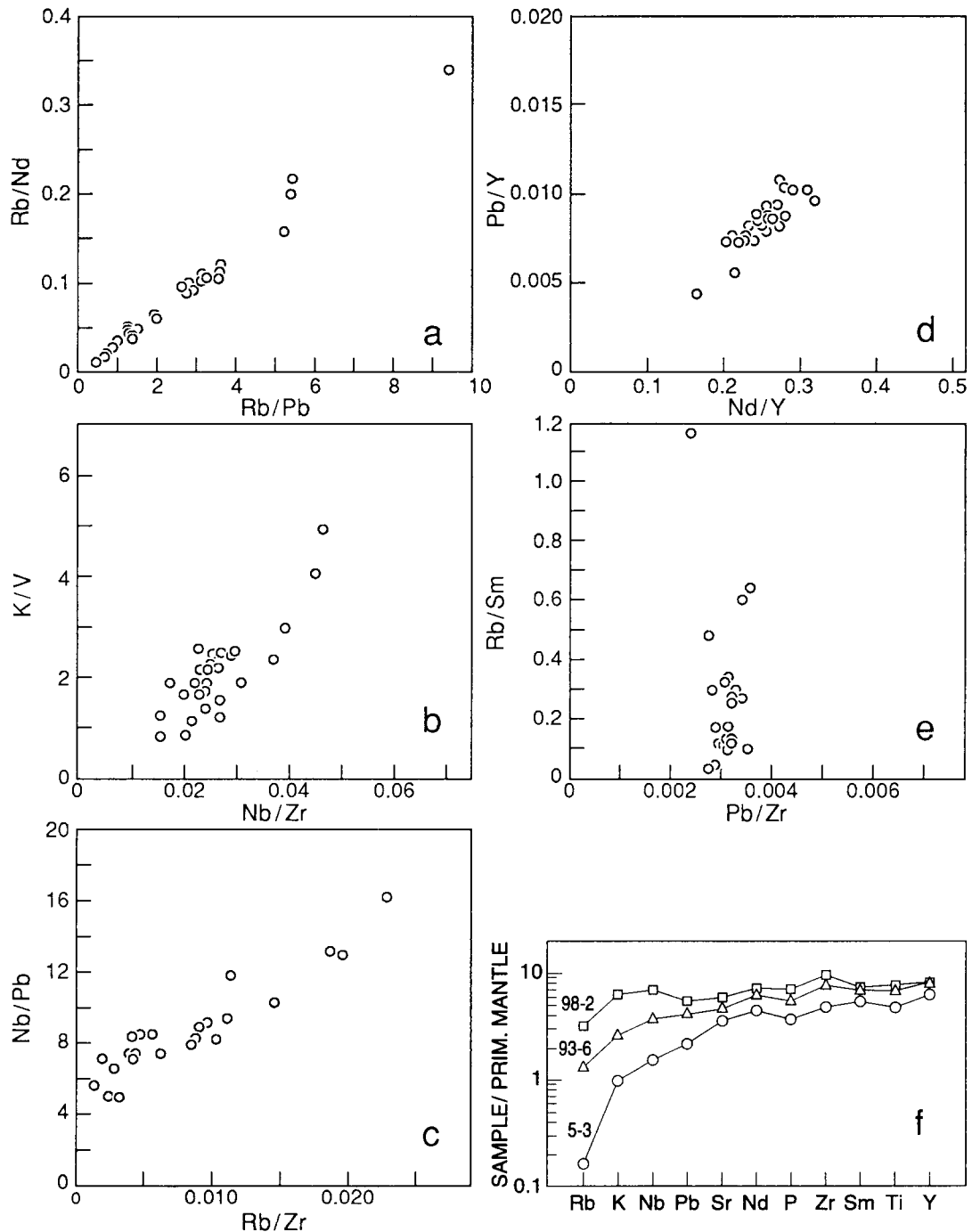


Fig. 8. (a–e) Selected plots of incompatible element variations among 13°–23°S lavas: (a) Rb/Nd vs. Rb/Pb, (b) K/V vs. Nb/Zr, (c) Nb/Pb vs. Rb/Zr, (d) Pb/Y vs. Nd/Y, and (e) Rb/Sm vs. Pb/Zr. Co-variations among these and similar ratios generally follow the expected order of element incompatibility in the MORB mantle [e.g., 27], and suggest that Pb acts much like Nd and Zr. For example, Pb/Zr (e) is almost constant, despite large changes in Rb/Sm. See text for additional discussion. (f) Primitive-mantle-normalized incompatible-element patterns for the most incompatible-element-depleted southern N-MORB of Table 2 (MW5-3), a northern N-MORB (MW93-6), and a northern T-MORB (MW98-2). Normalizing values are from [27].

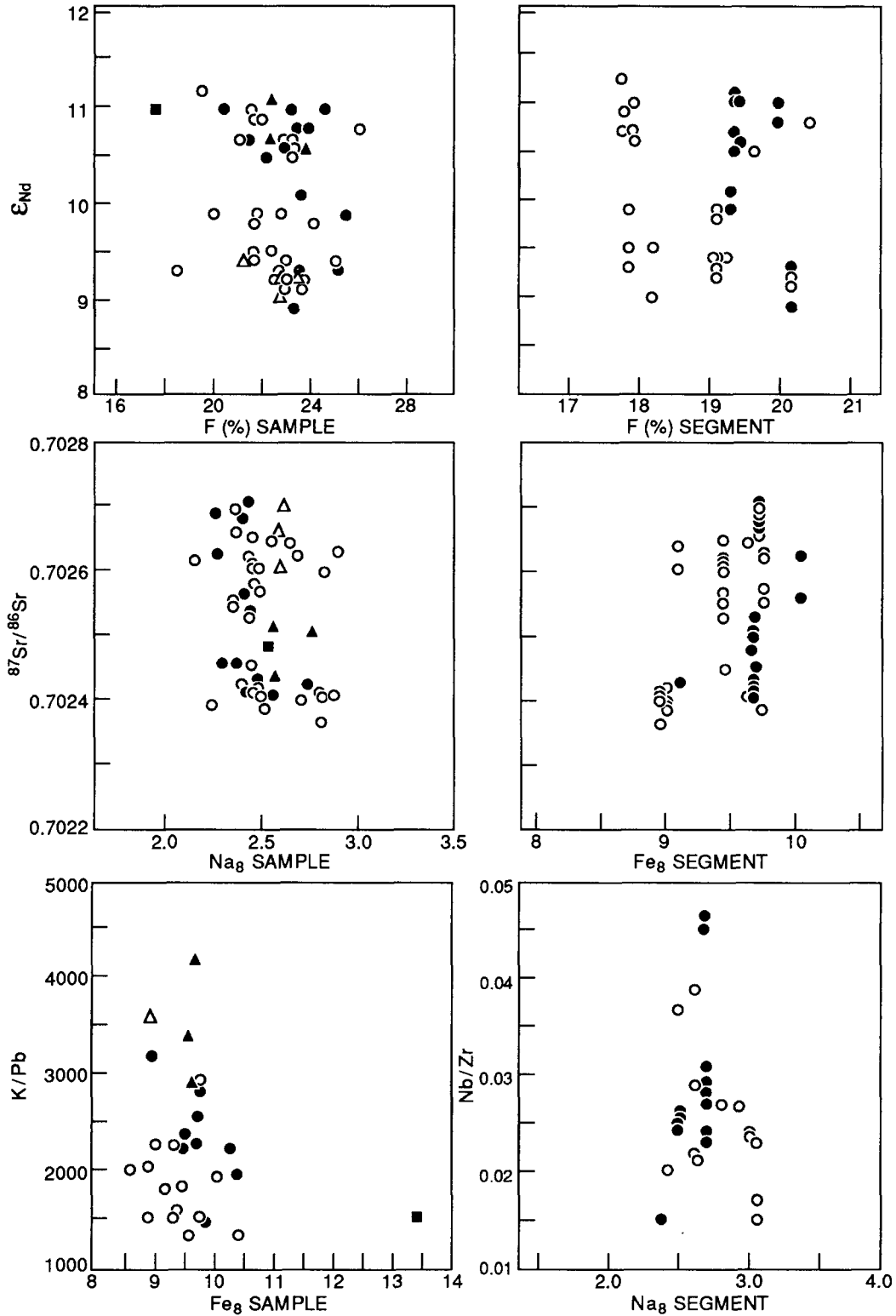


Fig. 9. Variation in the isotopic and incompatible element ratios (for individual samples) with fractionation-adjusted major element parameters for both the individual samples (panels on left) and the respective secondary magmatic segments to which they belong (panels on right).  $F$  = percentage of partial melting, as estimated from fractionation-adjusted major element abundances following [14].  $Fe_8$  (estimated total Fe as FeO at 8 wt% MgO) and  $Na_8$  (estimated  $Na_2O$  at 8 wt% MgO) calculated as described in [7]. Symbols are as in Fig. 7 for panels on the left and as in Fig. 3 for panels on the right.

subaxial melting. The same must also be true on a regional scale, because at 13.1–15.8°S and 20.7–23°S the total range of along-axis isotopic variation is very limited over distances of 250–300 km. Nonetheless, the slight Sr and Pb isotopic differences between some of the T-MORBs and nearby N-MORBs, whose major elements do not appear to reflect dramatically different degrees of melting, show that small-scale isotopic heterogeneities do exist in the subaxial mantle.

Assuming the now conventional view of a streaky, blob-riddled, or veined mantle [e.g., 37–40], much of the observed isotopic uniformity is probably explained by enhanced solid-state mixing in the asthenosphere accompanying super-fast spreading rates. Small-scale homogenization, in particular, could result from the greater flux of material toward the subaxial melt zone compared to that at slower spreading rates. Another key factor is that at super-fast spreading the volume (although not necessarily the degree) of melting per unit time per unit length of ridge axis is greater than at slower spreading ridges, a feature that should tend to decrease isotopic variability between melts [e.g., 1 and references therein]. For example, off-ridge seamounts between 18°S and 19°S are isotopically somewhat more heterogeneous than adjacent axial lavas, probably because the seamount basalts reflect substantially smaller scales of melting, at which the mantle is not isotopically uniform [54; cf., 41,42].

To explain the regional-scale homogeneity at 13.1–15.8°S and 20.7–23°S, vigorous, widespread and longer-term convection appears necessary; higher mantle mixing rates are likely to be associated with high plate velocities, at least at shallow levels in the asthenosphere where coupling is greatest. Plate migration rates in the southern Pacific area have frequently been high to very high since the Early Cretaceous or even earlier [e.g., 43], and so appear quite compatible with enhanced convective asthenospheric mixing over a long period of time. Fairly prolonged, enhanced mixing may also account for the observation of identical isotopic signatures at both the super-fast spreading section of the East Pacific Rise at 30–34.5°S and the slower spreading northern Maddingley Rise to the east of it, which (in part)

led Macdougall and Lugmair [1,6] to doubt a relationship between spreading rate and isotopic variability. Even prolonged convection, however, has been unable to erase larger mantle domains, as shown by the difference in  $^{207}\text{Pb}/^{204}\text{Pb}$  between the 13.1–15.8°S and 20.7–23°S lavas, which probably reflects long-term isolation of their sources from each other. Finally, in addition to efficient convective mixing, some of the isotopic uniformity in our study area may be intrinsic, owing to a scarcity in the MORB mantle of (originally) continental lithospheric, recycled slab, or plume-type material with extreme isotopic signatures, such as the low  $^{206}\text{Pb}/^{204}\text{Pb}$ , high  $^{87}\text{Sr}/^{86}\text{Sr}$  end-members so prevalent in the Indian Ocean (where, incidentally, some of the fastest spreading ever known occurred between ~80 and 40 m.y. ago) [11,20, and references therein]. The long-term absence of continents and continental breakup in the southeastern Pacific region [e.g., 43] is particularly noteworthy in this respect.

Significantly, there is (almost) nothing in our data to indicate that Pb isotopes behave in a fundamentally different fashion from Nd or Sr isotopes. This result runs counter to recent proposals by several authors [e.g., 4] and also contrasts with data for seven samples analyzed from 30–34.5°S where, as noted earlier, Pb isotopes vary while Nd and Sr isotopes remain nearly constant. There, the combination of relatively low  $\epsilon_{\text{Nd}}$  (~ +8.8),  $^{87}\text{Sr}/^{86}\text{Sr}$  (~ 0.70250), and high  $^{206}\text{Pb}/^{204}\text{Pb}$  (18.6–18.9) suggests to us that small but slightly different amounts of a Tubuaii- or Mangaia-like [44,45] end-member might be influencing the ambient MORB mantle composition. In hotspot-free regions at very slow spreading rates, such as on the Southwest Indian Ridge, Pb isotopes can also vary substantially with little corresponding change in Nd or Sr isotope ratios [e.g., 11]. In some regions, variable long-term radiogenic ingrowth in the mantle could account for such differences [cf.3], because the half lives of Th and U are relatively short and the parent-daughter ratios high in the source compared to the Rb–Sr and Sm–Nd systems. Moreover, in many parts of the world's ridge system an apparently independent variation of Pb relative to Nd and Sr isotopes probably arises from the simulta-



neous (but variable) influence in the N-MORB mantle matrix of both low- and high- $^{206}\text{Pb}/^{204}\text{Pb}$  mantle heterogeneities (for example, Easter-type [1,16] and Pitcairn-type [46]), which are all characterized by low  $\epsilon_{\text{Nd}}$  and high  $^{87}\text{Sr}/^{86}\text{Sr}$  compared to N-MORB mantle. Based on our results, it seems clear that in the absence of such complications, the behavior of Pb need not be notably different from that of Nd or Sr isotopes.

On the other hand, two features of our data suggest that Pb isotopes may not behave precisely like Nd or Sr isotopes. Firstly, despite the very good overall correspondence between isotopic ratios of all three elements, the variance in  $^{206}\text{Pb}/^{204}\text{Pb}$  and  $^{208}\text{Pb}/^{204}\text{Pb}$  over short spans of latitude—and regionally at 13.1–15.8°S and 20.7–23°S—tends to be greater relative to analytical error than for Sr or Nd isotopes (Table 1). As noted above, this result may partly reflect local time-integrated differences in parent–daughter ratios in the source because: (1) based on their values in basalts and probable melt–solid partitioning behavior,  $^{238}\text{U}/^{204}\text{Pb}$  and  $^{232}\text{Th}/^{204}\text{Pb}$  values are much larger than  $^{147}\text{Sm}/^{144}\text{Nd}$  and  $^{87}\text{Rb}/^{86}\text{Sr}$  in MORB source mantle (by more than one and two orders of magnitude, respectively); and (2) the half-lives of  $^{238}\text{U}$  and  $^{232}\text{Th}$  are considerably shorter than those of  $^{87}\text{Rb}$  or  $^{147}\text{Sm}$  (by factors of 3.5–24).

The second point relevant to Pb isotope expression is that the highly incompatible-element-depleted sample from the Garrett Fracture Zone (MW103-4) is unique in that its Pb isotopic values are much lower than any others analyzed, whereas its Nd and Sr isotope ratios are indistinguishable from those of the rest of the 13.1–15.8°S group. Its major elements suggest that it could represent a relatively small-degree melt (Fig. 10, top left panel and [7]); accordingly, its very low incompatible element abundances imply that it may be the residue of an earlier phase of melting, perhaps one that took place beneath the axis north of the fracture zone, given the location of this dredge haul. Its isotopic characteristics *could* suggest that some of the sites where Pb resides in the mantle source are different from those where Sr and Nd occur and, possibly, that the scale at which they are intermixed might be different, but

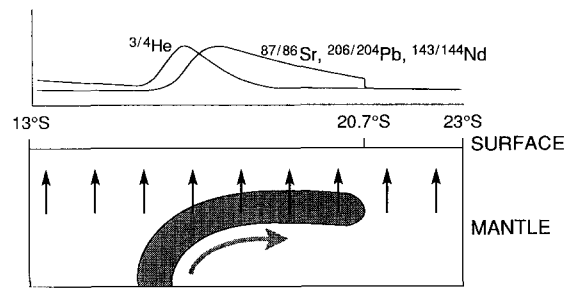


Fig. 10. Schematic diagram showing possible geometry of a heterogeneity (shaded) embedded in the N-MORB mantle matrix, entering into the subaxial melt zone (vertical arrows) and possessing a component of shallow along-axis motion (horizontal arrow). The isotopic curves above represent idealized latitudinal patterns. See text for explanation.

nothing definitive can be said based on only one anomalous sample.

#### 4.2. Meaning of regional isotopic patterns

The lower  $\epsilon_{\text{Nd}}$  and elevated Sr and Pb isotopic ratios culminating around 17–17.5°S (Fig. 2) are consistent with the presence of some hotspot- or plume-like material in the underlying mantle, although they do not necessarily demand it because they do not exceed values found elsewhere in normal MORBs. However,  $^3\text{He}/^4\text{He}$  ratios as high as the maximum observed are otherwise found only in association with hotspots or hotspot-affected regions and therefore provide strong evidence for plume-like material [53]. Interestingly, a broad increase in the cross-sectional area of the rise occurs between 16°S and 19°S, reaching a maximum around 17.5°S [47]; therefore, the peak in isotopic ratios probably corresponds to a region of enhanced production of crust and greater total volume of melting. Moreover, a large field of seamounts decorates the seafloor west of the axis between ~17°S and 19°S [48]. However, there is no evidence for a long-lived hotspot anywhere in the region.

One possibility is that a new plume could just be surfacing and coincidentally happens to be under or very near the axis in this area; but we consider it more likely that, instead, a discrete

heterogeneity containing material of plume-like isotopic composition lies embedded within the MORB mantle matrix. This material may very well have originated long ago in a plume associated with a distant hotspot but became separated and entrained into the MORB mantle flow field, eventually being transported to its present location. It may even have come from the Easter hotspot, for Easter Island and Sala y Gomez lavas exhibit Nd, Sr, and Pb isotopic ratios [e.g., 1,16,26] that plot along extensions of the arrays in Figs. 3–5 and may also have high  $^3\text{He}/^4\text{He}$  [49]. Alternatively, some lavas of the Marquesas hotspot, which lies to the west of the East Pacific Rise at  $\sim 8$ – $11^\circ\text{S}$ , also have roughly appropriate Nd, Sr, and Pb isotopic compositions [44,50]; the recently discovered ‘Pukapuka Ridge’ system, which extends from the seamount field west of the rise axis to just south of the Marquesas (D. Sandwell, unpubl. data, 1993), possibly points to a western Pacific connection. Note, however, that our data say nothing about the direction of approach of such a heterogeneity into the subaxial melt zone: it could be entering from directly below or from either side of the ridge axis. The fact that it does not express itself markedly in incompatible element ratios or major elements suggests that differences between the heterogeneity and the surrounding mantle are smaller than variations arising from magmatic and/or T-MORB-related enrichment processes; in particular, plume-type material may be significantly diluted with ambient high- $\epsilon_{\text{Nd}}$  mantle. Together with the lack of a clear latitudinal peak in the trace element data, the observation that the Nd, Sr and Pb isotopic ratios all remain within the global range of normal MORB suggests that a fairly large proportion of high- $\epsilon_{\text{Nd}}$ , non-plume-type mantle is present even at  $17^\circ\text{S}$ .

Based on the Pb, Nd, and Sr isotopic patterns, this heterogeneity does not extend farther south than the  $20.7^\circ\text{S}$  OSC or much farther north than  $\sim 15.8^\circ\text{S}$  (at least not within the zone of mantle contributing to axial magmas). The coincidence of the large  $20.7^\circ\text{S}$  OSC, which has been characterized by a net southward migration for at least the last 3 m.y. [9], with an isotopic discontinuity suggests: (1) that this offset is coupled to at least a

local boundary in the shallow asthenosphere; and (2) that the shallow asthenosphere in this area has had a component of southward (i.e., along-axis) motion for some time. The latitudinal isotopic gradients both to the north and south, away from the isotopic peak, provide strong evidence for mixing of regularly decreasing proportions of the plume-like end-member with ambient low  $^{87}\text{Sr}/^{86}\text{Sr}$ , low  $^{206}\text{Pb}/^{204}\text{Pb}$ , high  $\epsilon_{\text{Nd}}$  mantle material. Because the rise axis south of  $20.7^\circ\text{S}$  has higher  $^{207}\text{Pb}/^{204}\text{Pb}$  for a given  $^{206}\text{Pb}/^{204}\text{Pb}$  than that north of  $15.8^\circ\text{S}$  (Fig. 3a), as well as lower  $^3\text{He}/^4\text{He}$  (Fig. 2d and [54]), the northern and southern limbs of the isotopic peak in Fig. 2 are likely to reflect the involvement of two different high- $\epsilon_{\text{Nd}}$  end-members. Indeed, this is indicated by the slight separation between trends for lavas from north (dots) and south (circles) of  $17.3^\circ\text{S}$  in Figs. 3a, 4 and 5b–d. White et al. [3] also considered the possibility of binary mixing in the  $18.4$ – $20.7^\circ\text{S}$  area, but favored the view that Pb isotopic relations represented mantle isochrons with closed-system ages of  $\sim 2 \times 10^9$  yr, rather than mixing arrays. The much larger data set here clearly supports large-scale mixing in the  $15.8$ – $20.7^\circ\text{S}$  region; although, as pointed out in the previous section, the  $13.1$ – $15.8^\circ\text{S}$  and  $20.7$ – $23^\circ\text{S}$  high- $\epsilon_{\text{Nd}}$  mantle domains have probably long been isolated from each other.

The much narrower peak in  $^3\text{He}/^4\text{He}$  and its apparent offset, slightly to the north of the Sr, Nd, and Pb isotopic peaks, can be explained in the context of ridge-parallel motion in the shallow asthenosphere, which, as noted above, is strongly suggested by relations at the  $20.7^\circ\text{S}$  OSC. One possible scenario is depicted in Fig. 10, in which the heterogeneity is not only migrating into the subaxial melt zone near  $15.8^\circ\text{S}$  (again, not necessarily vertically; it could equally well be approaching from the west or east) but also moving southward at shallow mantle levels relative to the plate above. Assuming that He is substantially more incompatible than Nd, Sr, or Pb [e.g., 23] (either because of a much lower solid–melt partition coefficient or greater mobility in near-solidus but unmelted mantle), then He is preferentially and progressively extracted from the heterogeneity, such that by about  $18.5^\circ\text{S}$  no discernible

plume-like He isotope signal remains above the ambient MORB-type background value. Nd, Sr and Pb are not removed from the heterogeneity as effectively and some signal persists for them as far as its southern limit at 20.7°S. Recently, Poreda et al. [49] have also argued that a partial decoupling of He isotopes from those of Sr and Pb along the East Rift of the Easter Microplate may be explained in terms of lateral movement of plume-type mantle, only in their case the presumed motion is perpendicular to the axis (i.e., in a sublithospheric channel linking the rift to the off-ridge Easter hotspot).

In the framework of the model illustrated in Fig. 10, the fact that the latitudinal isotopic patterns for Sr, Nd, and Pb are in phase (within the ability of our data to resolve) and similar in overall shape is mainly a consequence of roughly similar distribution coefficients for these three elements during melting. Furthermore, the Sr/Nd, Pb/Nd and Pb/Sr values in the (unmelted) plume-like and high- $\epsilon_{\text{Nd}}$  end-members must not be drastically different; in a general way, this is suggested by the absence of marked, systematic differences in these ratios among the northern, central and southern portions of the study area (e.g., Fig. 6c) and by the absence of pronounced curvature in the isotopic arrays of Figs. 4 and 5. As noted earlier, our elemental abundance data indeed indicate that Nd and Pb have very similar incompatibilities. Unfortunately, Sr has been somewhat decoupled from the other incompatible elements by variable plagioclase fractionation, so a detailed, independent assessment of the relative incompatibility of Sr prior to magmatic differentiation cannot be made from trace element ratios. Intriguingly, though, the southern flank of the latitudinal peak in Sr isotopes (Fig. 2c) is slightly steeper than those for Nd or Pb isotopes (note that this is not an artifact of scaling) and, on the left or northern flank,  $^{87}\text{Sr}/^{86}\text{Sr}$  starts to increase one dredge station before Pb or Nd isotopes do. These differences are subtle and do not greatly exceed analytical uncertainty but, in the context of the above model, *could* be taken to mean that Sr is slightly more incompatible during melting in this region than Nd or Pb.

## 5. Acknowledgments

Cruise MW8712 and analytical work at SOEST were supported by NSF grants OCE86-0880 and OCE89-22978 to JMS and JJM; work at Scripps was funded by NSF grants to JDM and GWL, and He isotopes were analyzed at WHOI under NSF OCE grants to MDK. We thank reviewers P. Castillo, B. Hanan and P. Michael, as well as R. Hekinian for the Cyana samples, H. Craig for the Vulcan sample, and C. Koyanagi and N. Hulbert for typing and illustrations. SOEST contribution 3284.

## 6. References

- [1] J.D. Macdougall and G.W. Lugmair, Sr and Nd isotopes in basalts from the East Pacific Rise: significance for mantle heterogeneity, *Earth Planet. Sci. Lett.* 77, 273–284, 1986.
- [2] E. Ito, W.M. White and C. Göpel, The O, Sr, Nd and Pb isotope geochemistry of MORB, *Chem. Geol.* 62, 157–176, 1987.
- [3] W.M. White, A.W. Hofmann and H. Puchelt, Isotope geochemistry of Pacific mid-ocean ridge basalt, *J. Geophys. Res.* 92, 4881–4893, 1987.
- [4] M.B. Holness and F.M. Richter, Possible effects of spreading rate on MORB isotopic and rare earth composition arising from melting of a heterogeneous source, *J. Geol.* 97, 247–260, 1989.
- [5] C. DeMets, R.G. Gordon, D.F. Argus and S. Stein, Current plate motions, *Geophys. J. Int.* 101, 425–478, 1990.
- [6] J.D. Macdougall and G.W. Lugmair, Extreme isotopic homogeneity among basalts from the southern East Pacific Rise: mantle or mixing effect?, *Nature* 313, 209–211, 1985.
- [7] J.M. Sinton, S.M. Smaglik, J.J. Mahoney and K.C. Macdonald, Magmatic processes at superfast spreading mid-ocean ridges: glass compositional variations along the East Pacific Rise 13°–23°S, *J. Geophys. Res.* 96, 6133–6155, 1991.
- [8] C.H. Langmuir, J.F. Bender and R. Batiza, Petrological and tectonic segmentation of the East Pacific Rise, 5°30′–14°30′N, *Nature* 322, 422–429, 1986.
- [9] K.C. Macdonald, R.M. Haymon, S.P. Miller, J.-C. Semperé and P.J. Fox, Deep-tow and Sea Beam studies of dueling propagating ridges on the East Pacific Rise near 20°40′S, *J. Geophys. Res.* 93, 2875–2898, 1988.
- [10] K.H. Rubin, J.D. Macdougall, J.M. Sinton and J.J. Mahoney, U-series disequilibrium and Th isotope studies of East Pacific Rise MORB from 13°–23°S: axial variations

- in age, source region chemistry and trace element fractionation, *Earth Planet. Sci. Lett.*, in revision, 1993.
- [11] J. Mahoney, A.P. Le Roex, Z. Peng, R.L. Fisher and J.H. Natland, Southwestern limits of Indian Ocean ridge mantle and the origin of low  $^{206}\text{Pb}/^{204}\text{Pb}$  mid-ocean ridge basalt: isotope systematics of the central Southwest Indian Ridge (17°–50°E), *J. Geophys. Res.* 97, 19,771–19,790, 1992.
  - [12] K. Norrish and B.W. Chappell, X-ray fluorescence spectrometry, in: J. Zussman, ed., *Physical Methods in Determinative Mineralogy*, 2nd edition, pp. 201–272, Academic Press, New York, 1977.
  - [13] C.H. Langmuir and J.F. Bender, The geochemistry of oceanic basalts in the vicinity of transform faults: observations and implications, *Earth Planet. Sci. Lett.* 69, 107–127, 1984.
  - [14] Y. Niu and R. Batiza, An empirical method for calculating melt compositions produced beneath mid-ocean ridges: application for axis and off-axis (seamounts) melting, *J. Geophys. Res.* 96, 21,753–21,777, 1991.
  - [15] R.N. Yonover, Petrological effects of rift failure at the Galapagos spreading center near 95.5°W, including analyses of glass inclusions by laser mass spectrometry and ion microprobe, Ph.D. Thesis, Univ. Hawaii, 1989.
  - [16] B.B. Hanan and J.-G. Schilling, Easter Microplate evolution: Pb isotope evidence, *J. Geophys. Res.* 94, 7432–7448, 1989.
  - [17] M.D. Kurz, W.J. Jenkins and S.R. Hart, Helium-isotopic systematics of oceanic islands and mantle heterogeneity, *Nature* 297, 43–46, 1982.
  - [18] M.D. Kurz, W.J. Jenkins, J.-G. Schilling and S.R. Hart, Helium isotope variations in the mantle beneath the North Atlantic Ocean, *Earth Planet. Sci. Lett.* 58, 1–4, 1982.
  - [19] R. Poreda, J.-G. Schilling and H. Craig, Helium and hydrogen isotopes in ocean-ridge basalts north and south of Iceland, *Earth Planet. Sci. Lett.* 78, 1–17, 1986.
  - [20] J.J. Mahoney, J.H. Natland, W.M. White, R. Poreda, S.H. Bloomer, R.L. Fisher and A.N. Baxter, Isotopic and geochemical provinces of the western Indian Ocean spreading centers, *J. Geophys. Res.* 94, 4033–4052, 1989.
  - [21] D.W. Graham, W.J. Jenkins, J.-G. Schilling, G. Thompson, M.D. Kurz and S.E. Humphries, Helium isotope geochemistry of mid-ocean ridge basalts from the South Atlantic, *Earth Planet. Sci. Lett.* 110, 133–147, 1992.
  - [22] H. Craig and J.E. Lupton, Primordial neon, helium and hydrogen in oceanic basalts, *Earth Planet. Sci. Lett.* 31, 369–385, 1976.
  - [23] M.D. Kurz, Mantle heterogeneity beneath oceanic islands: some inferences from isotopes, *Philos. Trans. R. Soc. London Ser. A* 342, 91–103, 1993.
  - [24] S.P. Verma, J.-G. Schilling and D.G. Wagoner, Neodymium isotopic evidence for Galapagos-spreading centre system evolution, *Nature* 306, 654–657, 1983.
  - [25] B.B. Hanan, R.H. Kingsley and J.-G. Schilling, Pb isotope evidence in the South Atlantic for migrating ridge-hotspot interactions, *Nature* 322, 137–144, 1986.
  - [26] D. Fontignie and J.-G. Schilling,  $^{87}\text{Sr}/^{86}\text{Sr}$  and REE variations along the Easter Microplate boundaries (South Pacific): application of multivariate statistical analyses to ridge segmentation, *Chem. Geol.* 89, 209–241, 1991.
  - [27] S.-S. Sun and W.F. McDonough, Chemical and isotopic systematics of oceanic basalts: implications for mantle composition and processes, in: A.D. Saunders and M.J. Norry, eds., *Magmatism in the Ocean Basins*, *Geol. Soc. London Spec. Publ.* 42, 313–345, 1989.
  - [28] A. Meijer, T.-T. Kwon and G.R. Tilton, U–Th–Pb partitioning behavior during partial melting in the upper mantle: implications for the origin of high  $\mu$  components and the “Pb paradox”, *J. Geophys. Res.* 95, 433–448, 1990.
  - [29] D. McKenzie and R.K. O’Nions, Partial melt distributions from inversion of rare earth element concentrations, *J. Petrol.* 32, 1021–1091, 1991.
  - [30] Z. Qin, Disequilibrium partial melting model and its implications for trace element fractionations during mantle melting, *Earth Planet. Sci. Lett.* 112, 75–90, 1992.
  - [31] A.W. Hofmann, K.P. Jochum, M. Seufert and W.M. White, Nb and Pb in oceanic basalts: new constraints on mantle evolution, *Earth Planet. Sci. Lett.* 79, 33–45, 1986.
  - [32] W.M. White,  $^{238}\text{U}/^{204}\text{Pb}$  in MORB and open system evolution of the depleted mantle, *Earth Planet. Sci. Lett.* 115, 211–226, 1993.
  - [33] E.M. Klein and C.H. Langmuir, Global correlations of ocean ridge basalt chemistry with axial depth and crustal thickness, *J. Geophys. Res.* 92, 8089–8115, 1987.
  - [34] P.M. Kenyon, Trace element and isotopic effects arising from magma migration beneath mid-ocean ridges, *Earth Planet. Sci. Lett.* 101, 367–378, 1990.
  - [35] R. Batiza, Inverse relationship between Sr isotope diversity and rate of oceanic volcanism has implications for mantle heterogeneity, *Nature* 309, 440–441, 1984.
  - [36] J.M. Sinton and R.S. Detrick, Mid-ocean ridge magma chambers, *J. Geophys. Res.* 97, 197–216, 1992.
  - [37] G.N. Hanson, Geochemical evolution of the suboceanic mantle, *J. Geol. Soc. London* 134, 235–253, 1977.
  - [38] D.A. Wood, A variably veined suboceanic upper mantle—genetic significance for mid-ocean ridge basalts from geochemical evidence, *Geology* 7, 499–503, 1979.
  - [39] J.G. Fitton and D. James, Basic volcanism associated with intraplate linear features, *Philos. Trans. R. Soc. London Ser. A* 317, 253–266, 1986.
  - [40] C.J. Allègre and D.L. Turcotte, Implications of a two-component marble-cake mantle, *Nature* 323, 123–127, 1986.
  - [41] A. Zindler, H. Staudigel and R. Batiza, Isotope and trace element geochemistry of young Pacific seamounts: implications for the scale of upper mantle heterogeneity, *Earth Planet. Sci. Lett.* 70, 175–195, 1984.
  - [42] P. Castillo and R. Batiza, Strontium, neodymium and lead isotope constraints on near-ridge seamount production beneath the South Atlantic, *Nature* 342, 262–265, 1989.

- [43] C.Y. Yan and L.W. Kroenke, A plate tectonic reconstruction of the Southwest Pacific, 0–100 Ma, *Proc. ODP Sci. Results* 130, 697–709, 1993.
- [44] P. Vidal, C. Chauvel and R. Brousse, Large mantle heterogeneity beneath French Polynesia, *Nature* 307, 536–538, 1984.
- [45] Z.A. Palacz and A.D. Saunders, Coupled trace element and isotope enrichment in the Cook-Austral–Samoa islands, Southwest Pacific, *Earth Planet. Sci. Lett.* 79, 270–280, 1986.
- [46] J.D. Woodhead and M.T. McCulloch, Ancient seafloor signals in Pitcairn Island lavas and evidence for large amplitude, small length-scale mantle heterogeneities, *Earth Planet. Sci. Lett.* 94, 257–273, 1989.
- [47] D.S. Scheirer and K.C. Macdonald, The variation in cross-sectional area of the axial ridge along the East Pacific Rise: evidence for the magmatic budget of a fast-spreading center, *J. Geophys. Res.* 98, 7871–7885, 1993.
- [48] Y. Shen, D.W. Forsyth, D.S. Scheirer and K.C. Macdonald, Two forms of volcanism: implications for the volume of off-axis crustal production on the west flank of the East Pacific Rise, *J. Geophys. Res.*, in press, 1993.
- [49] R.J. Poreda, J.-G. Schilling and H. Craig, Helium isotope ratios in Easter Microplate basalts, *Earth Planet. Sci. Lett.*, in press, 1993.
- [50] R.A. Duncan, M.T. McCulloch, H.G. Barszczus and D.R. Nelson, Plume versus lithospheric sources for melts at Ua Pou, Marquesas Islands, *Nature* 322, 534–538, 1986.
- [51] W. Todt, R.A. Cliff, A. Hanser and A.W. Hofmann,  $^{202}\text{Pb} + ^{205}\text{Pb}$  double spike for lead isotopic analysis, *Terra Cognita* 4, 209, 1984.
- [52] K. Govindaraju, 1989 compilation of working values and sample descriptions for 272 geostandards, *Geostand. Newsl.* 13, 1–113, 1989.
- [53] M.D. Kurz et al., in prep., 1993.
- [54] Waggoner et al., in prep., 1993.